energies

MDPI

Article

Heat Control Effect of Phase Change Microcapsules upon Cement Slurry Applied to Hydrate-Bearing Sediment

Guokun Yang [1], Tianle Liu [1,*], Hai Zhu [1], Zihan Zhang [1], Yingtao Feng [2], Ekaterina Leusheva [3] and Valentin Morenov [3]

[1] Faculty of Engineering, China University of Geosciences, Wuhan 430074, China; 1345781296@cug.edu.cn (G.Y.); zss9223@cug.edu.cn (H.Z.); cugzzh@cug.edu.cn (Z.Z.)
[2] Institute of Oilfield Chemistry, CNOOC Oil Service Co., Ltd., Sanhe 065201, China; fengyt@cosl.com.cn
[3] Department of Oil and Gas, Saint Petersburg Mining University, 199106 Saint Petersburg, Russia; leusheva_el@pers.spmi.ru (E.L.); morenov@spmi.ru (V.M.)
* Correspondence: yanggk@cug.edu.cn

Abstract: This study aims to develop a novel low-heat cement slurry using phase change microcapsule additives to reduce the decomposition of hydrate-bearing sediments during cementing. Microcapsules were prepared by coating mixed alkanes with polymethyl methacrylate, and lipophilic-modified graphite was incorporated to enhance the thermal conductivity of microcapsules. The effects of microcapsules upon the hydration heat, pore distribution, and compressive strength of the cement slurry/stone were studied through a variety of tests. The results showed that the phase-change temperature, thermal enthalpy, and encapsulation efficiency of the microcapsules were 8.99–16.74 °C, 153.58 Jg^{-1}, and 47.2%, respectively. The introduction of lipophilic-modified graphite reduced the initial phase-change temperature of microcapsules by 0.49 °C, indicating an improvement in their temperature sensitivity. The maximum hydration heat of cement slurry decreased by 41.3% with 7% dosage of microcapsules; the proposed microcapsules outperformed comparable low-heat additives. Moreover, the presence of microcapsules could reduce the number of large pores in (and thereby improve the compressive strength of) cement stone. The innovation of this study is that it comprehensively and intuitively confirms the feasibility of the application of low-heat cement slurry with MPCM as the key in hydrate sediments rather than just focusing on the reduction of hydration heat; furthermore, a self-made cementing device was developed to simulate the cementing process of hydrate deposition. The results show that the thermal regulation of microcapsules inhibited the temperature increase rate of the cement slurry, significantly reducing the damage caused to the hydrate. These findings should improve the safety and quality of cement in offshore oil and gas well applications.

Keywords: microencapsulated phase-change materials; heat control; temperature sensitivity; cementing; hydration heat; natural gas hydrate-bearing sediment

Citation: Yang, G.; Liu, T.; Zhu, H.; Zhang, Z.; Feng, Y.; Leusheva, E.; Morenov, V. Heat Control Effect of Phase Change Microcapsules upon Cement Slurry Applied to Hydrate-Bearing Sediment. *Energies* **2022**, *15*, 4197. https://doi.org/10.3390/en15124197

Academic Editor: Andrea Frazzica

Received: 16 May 2022
Accepted: 6 June 2022
Published: 7 June 2022

1. Introduction

In offshore oil and gas well cementing, natural gas hydrate-bearing sediment (GHBS) is often present at the well hole. The hydration heat released during the consolidation of cement slurry changes the stable phase equilibrium state of the hydrate (i.e., to a high pressure and low temperature) [1–3]. When this occurs, the gasified natural gas hydrate enters the cement slurry, which affects the sealing quality of the unhardened cement sheath [4]. In serious cases, the cementing operation may not succeed and a blowout accident could occur [5,6]. Therefore, to prevent accidents and ensure cementing quality in offshore cementing engineering, a cement slurry with a hydration-heat regulation function is urgently required [7,8]. One logical solution to this problem is to introduce phase-change materials (PCMs) as admixtures into the cement slurry, which would adjust its heat of hydration.

Owing to their ability to release or absorb heat during phase changes, and thereby maintain a stable system temperature, PCMs have been implemented in numerous other fields including thermal energy storage [9–11]. PCMs have been introduced as an additive to adjust the heat release rate of concrete with the aim of suppressing temperature cracks and achieved remarkable results [12,13]. However, the increase in fluidity of PCMs during phase change brings hidden danger to the safety of building gel materials [14,15]. Microencapsulated PCMs (MPCMs), which comprise a PCM (as the core material) encapsulated in a dense polymer or insoluble precipitation, are typically applied to address this problem, not only to retain a stable PCM shape during phase transitions but also to avoid incompatibility between the PCM and cement gel materials [16–18]. Usually, the phase change materials in MPCMs can be divided into two categories: inorganic hydrates and organic matter (such as alkanes, fatty alcohols, and fatty acids). Due to the characteristics of hydrated salt removing bound water step by step, when it is used as a PCM, it often has a wide temperature control range. For example, disodium hydrogen phosphate dodecahydrate can store heat in the temperature range of 25–75 °C [19]. In the process of offshore cementing, the cement slurry will experience the continuous changing temperature environment of 'seawater—GHBS—deep formation—GHBS', so the cement slurry additive is required to have excellent thermal stability. However, the well-known disadvantage of hydrate salt is that it is easy to precipitate and undercooled, which will damage its heat storage density in complex temperature environments. [20–22]. Compared with hydrated salts, organic PCMs exhibit better thermal stability [23–26]. Sari et al. [27] prepared MPCM by using heptadecane as a PCM, and tested its thermal stability. The results show that the latent heat of the prepared MPCM decreases by only 3.8% after 1000 phase transformations. Yu et al. [28] have also prepared PCMs with good thermal stability using octadecane as a PCM. However, their studies have pointed out that low thermal conductivity of organic compounds may reduce the sensitivity of MPCM to temperature. Furthermore, Liu et al. [29] microencapsulated paraffin with calcium carbonate as a shell to improve the temperature sensitivity of PCM by increasing the heating area of paraffin and the high thermal conductivity of calcium carbonate. Moreover, they tried to use MPCM to reduce the temperature rise rate of oil well cement slurry used in GHBS cementing. The results show that the hydration heat of cement slurry with 12 wt % MPCM decreases by 45.67%. To summarize, it seems feasible to introduce MPCMs into low-heat cement slurry as a more efficient heat-control additive, which might effectively avoid hydrate decomposition caused by high exothermic rates of cement slurry. In addition, to our knowledge, no clear research method has directly verified that the addition of MPCM will inhibit the damage of hydration heat of cement slurry on GHBS, which makes it obviously difficult to confirm the feasibility of MPCM application in this field.

In this study, a heat-control microcapsule (MPCM-1) with a mixed alkane core and polymethyl methacrylate (PMMA) shell was developed via in situ polymerization. The structures diagram of MPCM-1 is shown in Figure 1.

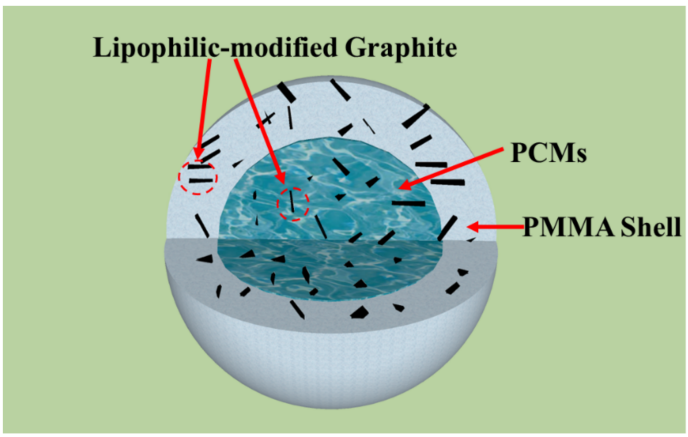

Figure 1. Structure diagram of MPCM-1.

Owing to the low thermal conductivity of alkanes and PMMA, lipophilic-modified graphite was introduced into MPCM-1 to improve its temperature sensitivity. Furthermore, the prepared MPCM-1 and other low-heat additive materials (e.g., fly ash, slag, and as-purchased MPCM) were added into the oil well cement slurry system to investigate their effects upon hydration temperature increase rates and maximum hydration heat. Based on the characteristic that gas channeling occurs easily during cementing in GHBS, the compressive strength and pore distribution of cement stone are studied, which are rarely focused on by other studies [29–31]. Finally, one of the innovations of this work is that a device to simulate the cementing process was designed, to intuitively evaluate the impact of low-heat cement slurry hydration upon the stability of hydrate-bearing sediments. This study verifies the feasibility of low-heat cement slurries containing phase-change microcapsules for safe cementing in hydrate-bearing sediments, which represents an important step forward in this area of research.

2. Experimental Section

2.1. Materials

N-tetradecane [analytical reagent grade (AR), 99%], n-hexadecane (AR, 98%), benzoyl peroxide (AR, 99%), polyvinyl alcohol (AR, 99%), and stearic acid (AR, 98%) were purchased from Aladdin Reagents (Shanghai, China) Co., Ltd. Aluminum chloride hexahydrate (AR, 97%) and absolute alcohol (AR, 99%) were purchased from Shanghai Meirel Chemical Technology Co., Ltd. (Shanghai, China). Microcrystalline graphite was purchased from Dingsheng Xin Chemical Co., Ltd. (Tianjin, China) Deionized water was self-made.

Class G oil-well cement and additives were provided by CNOOC (Sanhe, China) Co. Ltd. Fly ash and slag were purchased from Shanghai Weishen New Building Materials Co., Ltd. (Shanghai, China). The chemical compositions of Class G oil-well cement, fly ash, and slag are listed in Table 1.

Table 1. Chemical composition of cement, fly ash, and slag (%).

Sample	CaO	SiO_2	Al_2O_3	SO_3	K_2O	Na_2O	Fe_2O_3	TiO_2	CeO_2	LOI
Cement	64.10	20.10	3.67	3.54	0.62	0.29	4.89	0.31	-	3.10
Fly ash	6.69	52.45	29.35	0.74	1.07	0.89	5.93	1.24	0.20	4.41
Slag	34.66	30.04	13.54	0.83	0.31	0.33	0.31	0.57	0.14	0.39

In addition, several typical particle sizes are listed in Table 2.

Table 2. Particles size distribution of cement, fly ash, and slag (μm).

Sample	D_{10}	D_{50}	D_{90}
Cement	10.082	13.675	45.359
Fly ash	2.846	12.830	52.834
Slag	1.038	4.835	14.216

2.2. Synthesis of MPCM-1

2.2.1. Lipophilic Modification of Microcrystalline Graphite

First, 0.2 g stearic acid was dissolved in 20 mL absolute alcohol, and 0.22 g aluminum chloride hexahydrate was dissolved in 100 mL deionized water. The ethanol solution was then mixed with aqueous solution to form an emulsion, and 4 g microcrystalline graphite was added. The mixture was placed in a water bath with a temperature of 60 °C and stirred continuously at a rate of 100 r/min for 1.5 h. Finally, the modified microcrystalline graphite (with a rich lipophilic group on the surface) was obtained via suction filtration and drying. During this period, the filter material was not washed in order to prevent removal of the polymer material and suppression of its physical coating effect on the microcrystalline graphite during drying.

2.2.2. Synthesis of MPCM-1

First, 3 g polyvinyl alcohol was dissolved in 100 mL deionized water at 90 °C. Subsequently, 0.2 g benzoyl peroxide was dissolved in 10 mL methyl methacrylate (the inhibitor having been washed away by 1 wt% NaOH solution), and 0–0.8 g of lipophilic modified graphite (MG) was added and stirred evenly to produce a wall material solution (WM). Next, n-tetradecane and n-hexadecane were mixed and fused in a mass ratio of 1:4 to form 10 g of the phase change core material (i.e., the PCM). To prevent early polymerization of the methyl methacrylate (caused by high temperature or low temperature-induced solidification of PCM), the polyvinyl alcohol solution (100 mL), WM mixture (10 mL), and PCM solution (10 g) were kept at 50 °C for 10 min before being added together in a three-pot flask (500 mL). The water bath environment was then adjusted to 60 °C for 15 min (prepolymer process) and 80 °C for 1.5 h; the stirring speed was kept at 200 r/min. Finally, MPCM-1 was obtained by suction filtration, washing, and drying.

2.3. Characterization

The functional groups of the PCM, WM, and MPCM-1 were analyzed via FT-IR spectroscopy (Perkin Elmer Frontier, Perkin Elmer Co., Ltd., Waltham, USA) using the standard KBr disk method (scanning number: 32; optical range: 400–4000 cm^{-1}). The morphology of MPCM-1 without MG (MPCM-2) and MPCM-1 was observed using Zeiss stereoscopic optical microscopy (STEMI 508, Zeiss, Oberkochen, Germany). The NanoVoxel-3502E X-ray three-dimensional scanning system (micro-CT) (Sanying Precision Instrument Co., LT, Tianjin, China) was used to scan MPCM-1 (particle size > 200 mesh) placed in a cylindrical plastic mold. The core-wall structure of MPCM-1 (particle size > 200 mesh) was then assessed by analyzing the reconstructed MPCM-1 data using Voxel Studio Recon software (Sanying Precision Instrument Co., Ltd., Tianjin, China). A schematic diagram and digital photo of the micro-CT are shown in Figure 2.

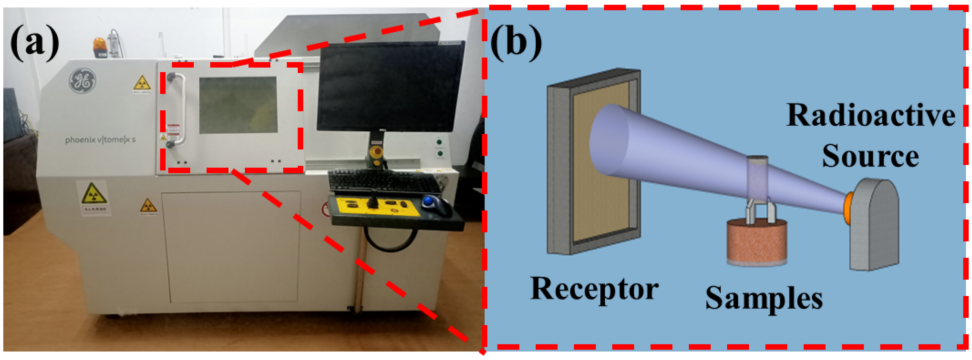

Figure 2. (**a**) Entity devices and (**b**) schematic diagram of micro-CT.

The microstructure of MPCM-1 (particle size < 200 mesh) and the element distribution upon its surface were observed using SEM (Carl Zeiss Sigma 300, Zeiss, Oberkochen, Germany) and energy-dispersive X-ray spectrometry (Smartedx, Zeiss, Oberkochen, Germany) after the MPCM-1 had been dispersed on a conductive adhesive and sprayed with gold powder. Using the transient plane heat source method, the thermal conductivity of WM (mass fractions: 0%, 2%, 4%, 6%, and 8% MG) fabricated into 5 × 5 × 0.05 cm^3 films was analyzed by Hot Disk (TPS 2500S, Kegonas Instrument Trading Co., Ltd., Shanghai, China) at 10 °C. Here, three samples in each group were tested; the average of each group was then taken as the final test result. The phase change performances of MPCM-1, PCM, and MPCM-2 (i.e., the phase change temperature and latent heat) were analyzed using DSC (DSC3, ETTLER TOLEDO, Zurich, Switzerland) at a heating/cooling rate of 5 °C/min in the range 0–60 °C under a nitrogen environment. A thermal analyzer (TGA55, ETTLER TOLEDO, Zurich, Switzerland) was used to analyze the thermal stability of MPCM-1 and PCM at a heating rate of 10 °C/min in the range 20–800 °C under a nitrogen environment, after which the samples were maintained at 800 °C for 30 min. The MPCM-1 (5 g) and PCMs (5 g) were

wrapped with dust-free blotting paper and placed in an electric blast drying oven. The samples were heated and cooled in 20 cycles over a temperature range of 0–60 °C. The samples were then weighed, and mass loss rate was calculated to estimate the thermal reliability of MPCM-1.

2.4. Preparation of Cement Slurry

First, the low-heat and low-density cement slurry applied to GHBS was prepared using the formula provided by the CNOOC Zhanjiang Branch (Sanhe, China); this was taken as the control group and denoted as "CS." Second, 10 wt% slag and 10 wt% fly ash were introduced into CS; the resulting samples were denoted as $CSS_{10\%}$ and $CSF_{10\%}$, respectively. Next, the 5 wt% phase change microcapsules (MPCM-3) purchased from Shanghai Feikang Products Factory were added into CS, and the result was denoted as $CSM_{5\%}$. Finally, 3.0 wt%, 5.0 wt%, and 7.0 wt% MPCM-1 were added into CS, and the resulting samples were denoted as $CSM1_{3\%}$, $CSM1_{5\%}$, and $CSM1_{7\%}$, respectively. The function of the additives and the design of the cement slurry system are shown in Tables 3 and 4.

Table 3. Functions of cement slurry additives.

Samples	X60L	F45L	G86L	BT5	P60
Function	Inhibit foam production	Improve rheological properties	Reduce water loss	Increase early strength	Reduce system density

Table 4. Mixture composition of cement slurry system (g).

Samples	Cement	Slag	Fly Ash	MPCM-1	MPCM	Water	X60L	F45L	G86L	BT5	P60
CS	600	-	-	-	-	1000	6	9	18	30	102
$CSS_{10\%}$	540	60	-	-	-	1000	6	9	18	30	102
$CSF_{10\%}$	540	-	60	-	-	1000	6	9	18	30	102
$CSM_{5\%}$	570	-	-	-	30	1000	6	9	18	30	102
$CSM1_{3\%}$	582	-	-	18	-	1000	6	9	18	30	102
$CSM1_{5\%}$	570	-	-	30	-	1000	6	9	18	30	102
$CSM1_{7\%}$	558	-	-	42	-	1000	6	9	18	30	102

The additives in all cement slurry samples were adjusted according to GB/T 19139-2012, and the density and rheological properties of the cement slurry are shown in Table 5.

Table 5. Physical properties of samples.

Samples	Density/g·cm^{-3}	Rheological Index	Consistency Coefficient (Pa·S^n)
CS	1.50	0.630	1.246
$CSS_{10\%}$	1.57	0.578	1.754
$CSF_{10\%}$	1.58	0.612	2.339
$CSM_{5\%}$	1.46	0.554	3.711
$CSM1_{3\%}$	1.48	0.598	1.874
$CSM1_{5\%}$	1.46	0.576	2.069
$CSM1_{7\%}$	1.45	0.561	2.154

2.5. Temperature and Hydration Heat of Cement Slurry

First, the cement slurry samples (shown in Table 4) were prepared and stirred at a high speed of 4000 r/min for 20 s and 12,000 r/min for 45 s. Before reaching the GHBS, the cement slurry passes through a low temperature (4 °C) region near the mud line. Hence, cement slurry samples were placed in a 4 °C curing tank for 15 min and transferred to a self-made semi-adiabatic calorimeter that met the GB/T12959-2008 standard and had a constant temperature of 8 °C. Fran bottles filled with the cement slurry were sealed with plasticine at the top, to reduce the effect of air temperature and to prevent water from

entering the cement paste. Finally, the changes in cement slurry temperature and hydration heat release over 48 h were recorded.

2.6. Compressive Strength of Cement Stone

Following the GB/T 17671-2021 standard, the cement slurry samples were placed into the standard mold (40 × 40 × 40 mm^3) and cured at a constant temperature in a humidity curing box (humidity: 90%) and at temperatures of 8 °C, 10 °C, and 15 °C for 24 h. The average compressive strengths of the three samples in each group were then measured using a compression and flexural testing machine (ZCYA-W300C, Star Fire Testing Machine Co., Ltd., Jinan, China).

2.7. Spatial Distribution of Pores and MPCM-1 in Cement Stone

First, the cement slurry samples were placed into a standard mold (20 × 20 × 20 mm^3) and cured in a constant temperature and humidity curing box (humidity: 90%; temperature: 8 °C) for 24 h. Micro-CT was then used to scan the spatial distribution of pores and MPCM-1 in cement stone. The dates were recorded after reconstruction using VG Studio Max software (scanning accuracy: 15.63 μm; voltage: 120 kV; current: 110 μA).

2.8. Simulation of GHBS Damage

The self-made device used to simulate the cementing process in the GHBS is shown in Figure 3. First, the simulated GHBS was formed by injecting methane gas into a formation cavity preloaded with 30 g of tetrahydrofuran, 770 mL of deionized water, and 8 kg of sand particles under increasing pressure and decreasing temperature. The cement slurry samples (800 mL) were injected into the slurry cavity. The damage of the simulated GHBS during cement slurry hydration was estimated using temperature and pressure sensors.

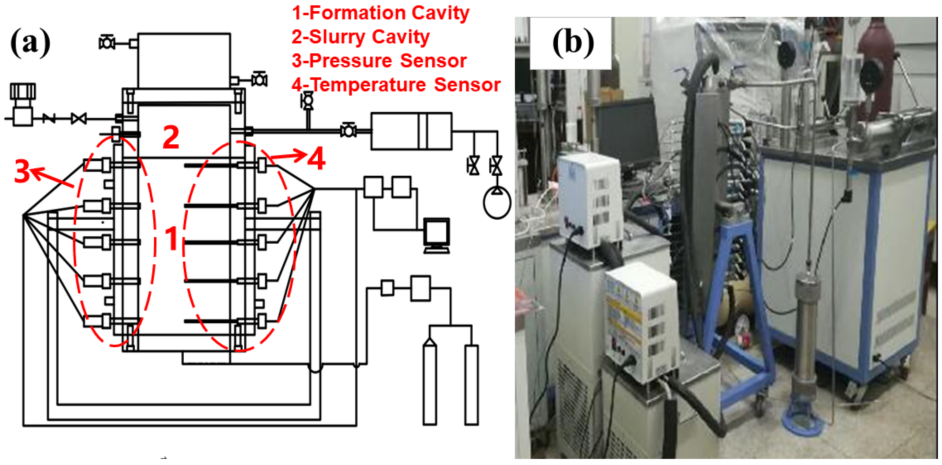

Figure 3. (**a**) Structure chart and (**b**) digital photo of device used to simulate cementing in GHBS.

3. Results and Discussion

3.1. Infrared Spectrum Analysis of MPCM-1

The infrared spectra of the PCM, WM, and MPCM-1 are shown in Figure 4.

For the FT-IR spectra of PCM, the absorption peak at 1464 cm^{-1} corresponds to the antisymmetric vibration of $-CH_3$, and the absorption peak at 720 cm^{-1} corresponds to the rocking vibration peak of $-(CH_2)_4$. In the infrared spectrum of WM, the strong absorption at 3429 cm^{-1} corresponds to the stretching vibration peak of −OH and −COOH dimer OH. The absorption peak at 1731 cm^{-1} corresponds to the umbrella bending vibration peak of $-CH_3$, and the absorption peak at 1270 cm^{-1} corresponds to the stretching vibration band of -O-C(O)-C [32]. Notably, the FT-IR spectrum of MPCM-1 contains all the characteristic absorption peaks of PCM and WM, and no new absorption peaks appear. Therefore, the preliminary results demonstrate that the energy storage density of the PCM has not been lost during microencapsulation, and MPCM-1 consists of PCM and WM.

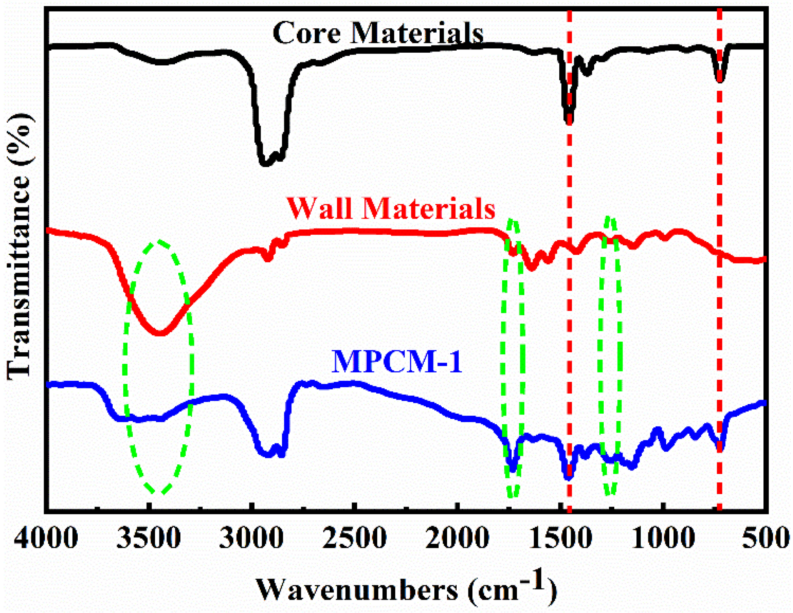

Figure 4. FTIR spectra of core materials (PCM), wall material (WM), and MPCM-1.

3.2. Microstructural Analysis of MPCM-1

Figure 5 shows the stereomicroscope views of MPCM-1.

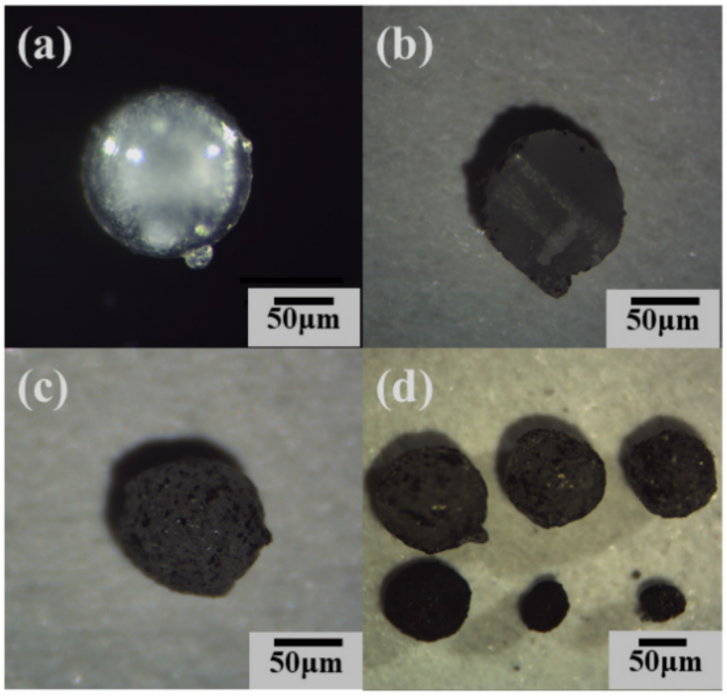

Figure 5. Stereomicroscope views of (**a**) MPCM-2, (**b**) MPCM-1 section, (**c**) MPCM-1, and (**d**) MPCM-1 of different sizes.

It can be observed from Figure 5 that the PCM was successfully encapsulated by the WM without the addition of MG. The 3D image model and slice images of MPCM-1 are presented in Figure 6. The images show that microcapsules combined with MG also exhibit an excellent core-wall structure; furthermore, the dense surface of WM helped to suppress PCM leakage during the phase transition.

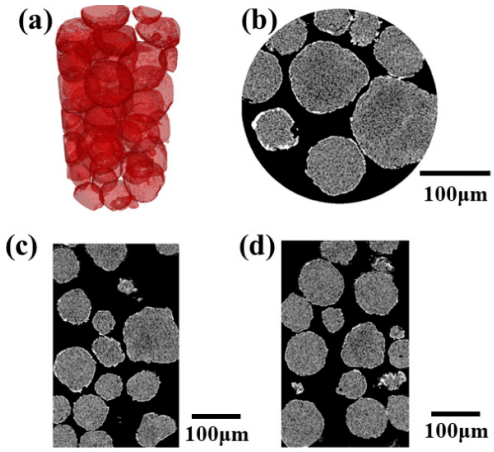

Figure 6. 3D image model and slice images of MPCM-1 (particle size > 200 mesh): (**a**) 3D image models, (**b**) XY plane slice, (**c**) YZ plane slice, and (**d**) XZ plane slice.

Besides this, the microcapsules prepared from the same batch with different particle sizes (Figure 5d) indicate that the mechanical strength of cement stone can be enhanced by varying the gradation relationship between the cement particles and MPCM-1, with suitable particle sizes isolated via screening [33–35]. The SEM micrographs of MPCM-1 (particle size < 200 mesh) are presented in Figure 7.

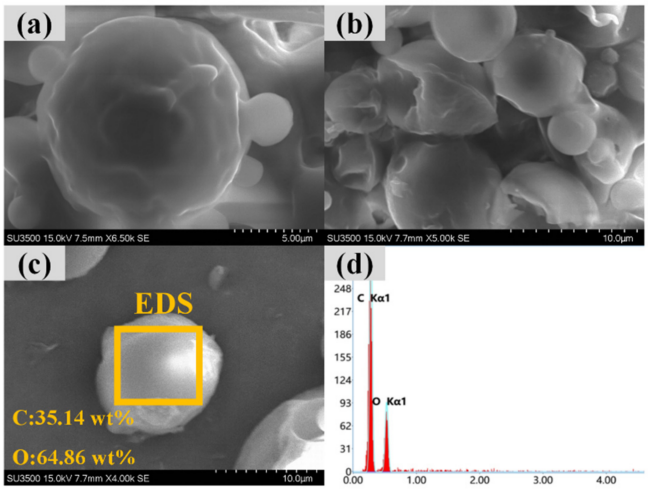

Figure 7. SEM micrographs of MPCM-1 (particle size < 200 mesh): (**a**) ×6500 and (**b**) ×5000. (**c**) EDS analysis. (**d**) Surface element content of MPCM-1.

The small-particle MPCM-1 appears easier to agglomerate but exhibits superior sphericity. The surface element content of MPCM-1 (shown in Figure 7c) demonstrates that the mass fractions of C and O are 35.14% and 64.86%, respectively; this conforms to the composition of C and O elements in the wall material (PMMA). Combined with the FT-IR analysis results, this provides strong evidence for the packaging effect of WM on PCMs, which allows them to satisfy design specifications.

3.3. Phase-Change Properties of MPCM-1

Thermal conductivity is an important factor in heat control; it affects temperature sensitivity and latent heat storage and release rates for MPCM-1 in the cement slurry. However, the thermal conductivity of organic PCMs is generally lower than that of cement slurry. In this study, the thermal conductivity of MPCM-1 was improved by adding microcrystalline graphite (which is inexpensive); furthermore, the lipophilic modification of

graphite was performed to evenly disperse it in MPCM-1. Figure 8 shows the compatibility of MG with water before and after lipophilic modification.

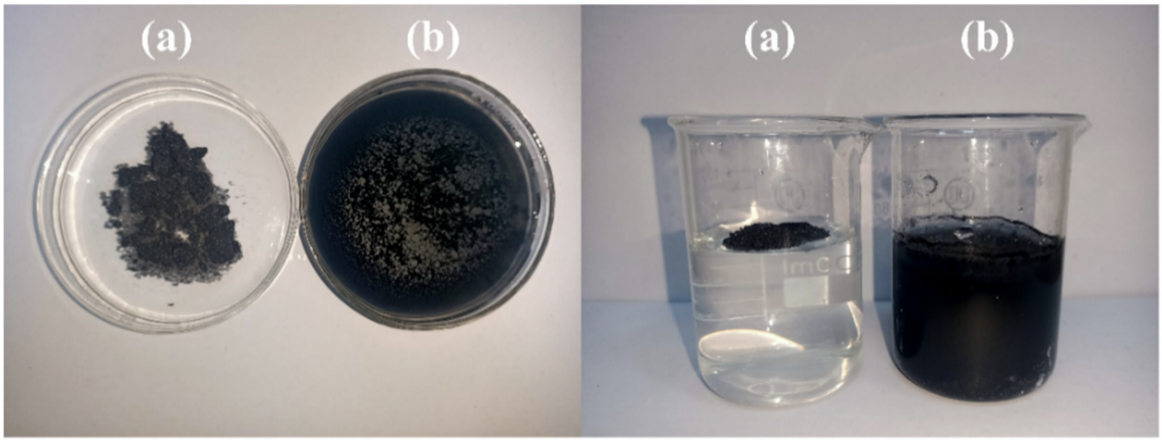

Figure 8. Comparison of hydrophobicity between (**a**) MG and (**b**) microcrystalline graphite.

The hydrophobicity of the MG increased markedly compared with that of the graphite, owing to the increase in the number of lipophilic groups on the surface. The improvement of MG lipophilicity was achieved via two stages: chemical modification and physical coating. The surface of the microcrystalline graphite contained hydroxyl groups [36,37] which could be esterified with stearic acid under aluminum chloride catalysis. By ester bonding, the carbon chain of stearic acid was partially distributed on the surface of the microcrystalline graphite, and the chemical modification was completed. During the drying process for microcrystalline graphite, the polymer (after esterification reaction) and stearic acid (without chemical reaction) were gradually precipitated out and coated on the surface of the microcrystalline graphite to produce a physical coating modification. Furthermore, the WM (with different mass fractions of MG) pressed into the films (as shown as Figure 9), and the hydrophobicity of the graphite after modification notably increased, allowing it to be uniformly dispersed in the WM.

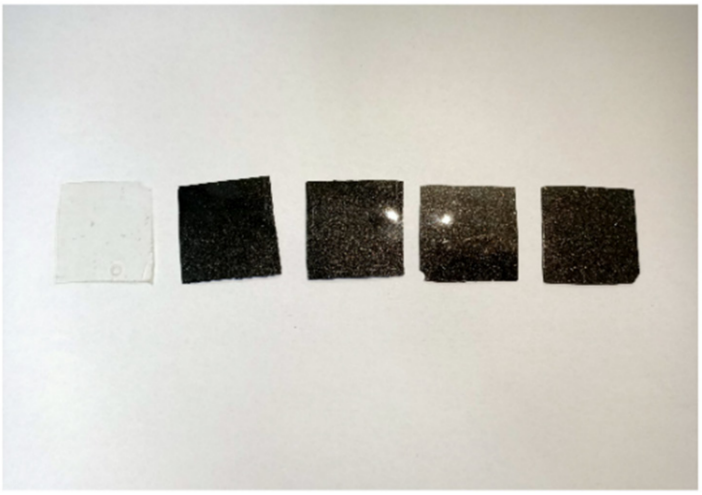

Figure 9. WM films at different MG dosages.

The thermal conductivity analysis of the WM is presented in Figure 10.

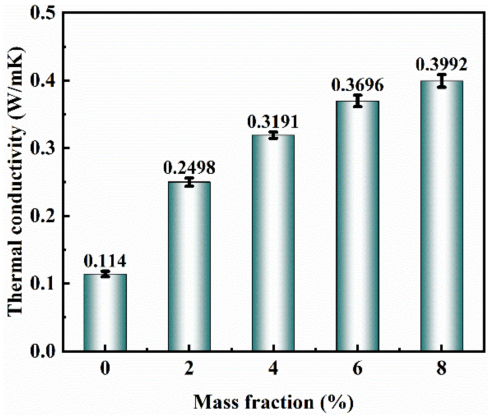

Figure 10. Thermal conductivity of WM films with modified MG.

Under the increase in MG mass fraction, the thermal conductivity of WM was considerably improved. However, MG entering the PCM reduced the PCM content per unit volume, lowering the thermal storage efficiency; therefore, a 4 wt% addition of MG was selected to optimally improve thermal conductivity.

The phase-change properties of PCM, MPCM-1, and MPCM-2 were tested, and the results are presented in Figure 11 and Table 6.

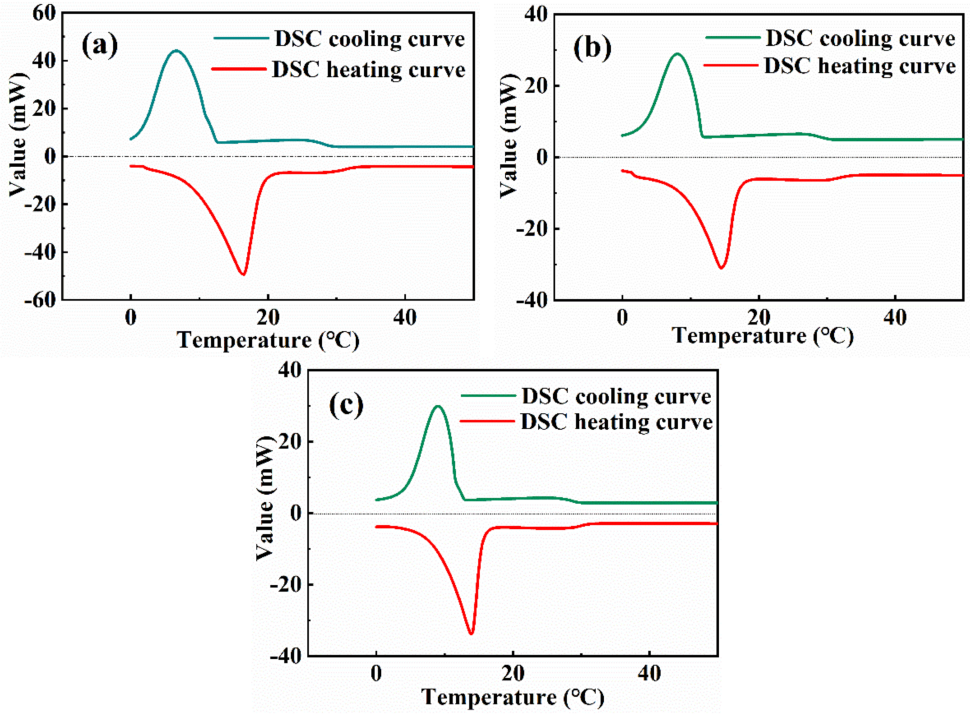

Figure 11. DSC curves of (**a**) PCM, (**b**) MPCM-1, and (**c**) MPCM-2.

Table 6. Phase-change behaviors.

Sample	Melting Process				Encapsulation Efficiency (%)
	T_o (°C)	T_p (°C)	T_e (°C)	ΔH_m (Jg^{-1})	
PCMs	9.01	15.32	18.82	325.34	
MPCM-1	8.99	13.77	16.74	153.58	47.2
MPCM-2	9.48	14.07	16.99	159.89	49.1

Both PCMs and MPCM-1 had high latent heat and a wide phase transition temperature range, owing to the mixed dissolution of n-tetradecane and n-hexadecane; this indicates that hydration heat was continuously absorbed by MPCM-1 over a large temperature range during the cement slurry hydration process. The phase-change temperature range, peak temperature, and latent heat of MPCM-1 were 8.99–16.74 °C, 13.77 °C, and 153.58 Jg^{-1}, respectively. Compared to MPCM-2, it is found that the initial phase-change temperature of MPCM-1 is 0.49 °C earlier, due to the addition of modified MG, and its temperature sensitivity was significantly enhanced. Moreover, only one phase transition peak appeared in each DSC curve, owing to the eutectic effect of the PCMs composed of n-tetradecane and n-hexadecane in this composition ratio during the phase transition process [20,38]. The formula for calculating the encapsulation efficiency E_e of MPCM-1 is [7,29]:

$$E_e = \frac{\Delta H_{m(MPCM-1)}}{\Delta H_{m(PCM)}} \times 100\% \quad (1)$$

where T_o, T_p, and T_e are the initial phase-change temperature, the peak phase-change temperature, and the end phase-change temperature in the melting process, respectively; ΔH_m is the latent heat during the melting process, for which $\Delta H_{m(MPCM-1)}$ and $\Delta H_{m(PCM)}$ are the latent heat of MPCM-1 and PCM during the melting process, respectively. Using this formula, the encapsulation efficiency of MPCM-1 is determined as 47.2% which may be lower than that of some other studies (the E_e is 67.8% and 66.5%, respectively) [7,29]; however, the lower encapsulation efficiency within a reasonable range ensures the ability of MPCM to resist external loads, which facilitates the mechanical strength of cement stone incorporated with *MPCM* [39].

3.4. Thermal Reliability of MPCM-1

Taking oil and gas resources in the South China Sea as an example, GHBS is typically present in the shallow surface of the mud line, with a water depth of 300–2000 m [40,41]. Cement slurry for deep-sea GHBS undergoes the following process: "seawater → GHBS → deeper formation → GHBS", during which the ambient temperature changes continually. In addition, MPCM-1 experiences frequent temperature variations during transport and storage on offshore platforms. The coating integrity of MPCM-1 under temperature change conditions is extremely important for ensuring its heat storage efficiency and the sealing performance of cement sheaths, which may be affected by PCM leakage. Hence, the thermal reliability of MPCM-1 was analyzed via TG and thermal cycles.

TGA and DTG curves of MPCM-1 and PCMs are shown in Figure 12.

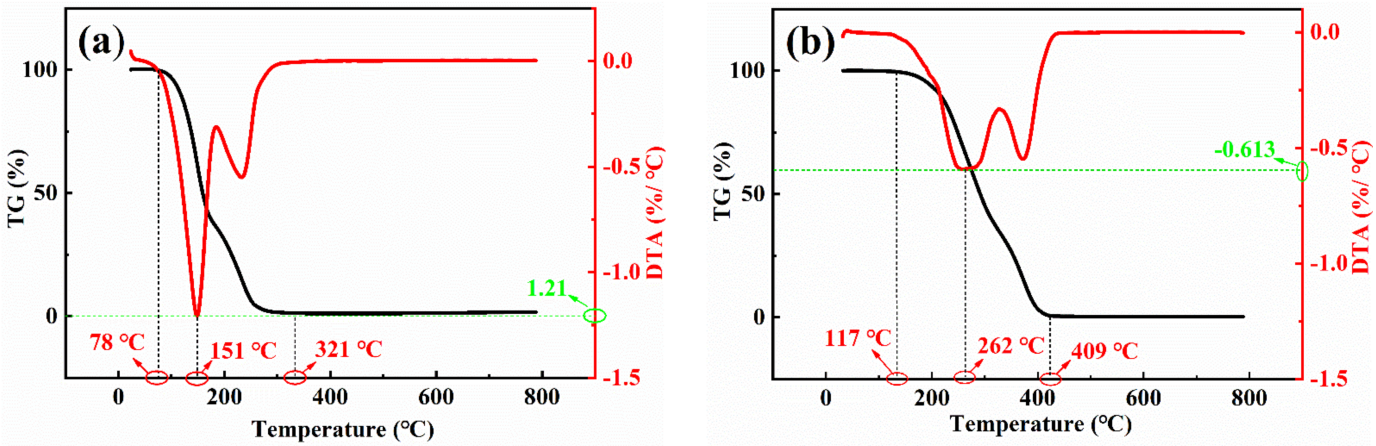

Figure 12. TGA curve and DTG curve of (**a**) PCM and (**b**) MPCM-1.

It can be observed that the initial and total mass loss temperatures of MPCM-1 were 117 °C and 409 °C, respectively; furthermore, when the temperature reached 262 °C, the

mass loss rate was maximized at 0.613/°C. Compared with PCMs, the initial and maximum mass loss rates of MPCM-1 were higher and slower, respectively, because of the coating effect of the WM on the PCMs [42].

The samples of the thermal cycle experiment are shown in Figure 13, and the test results are shown in Table 7.

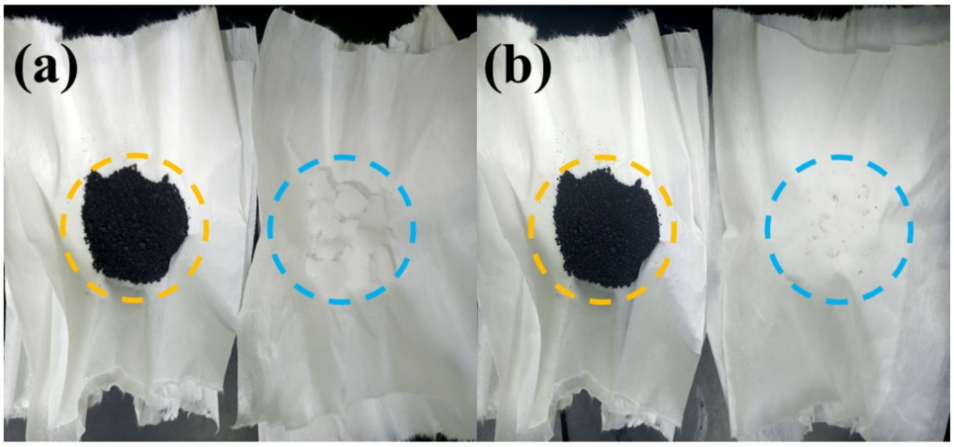

Figure 13. Digital photographs of (**a**) initial samples and (**b**) samples after thermal cycles.

Table 7. Mass loss of MPCM-1.

Sample	Initial Mass (g)	Mass after 5 Cycles (g); Mass Loss Rate (%)	Mass after 10 Cycles (g); Mass Loss Rate (%)	Mass after 15 Cycles (g), Mass Loss Rate (%)	Mass after 20 Cycles (g), Mass Loss Rate (%)
MPCM-1	5	4.5, 10	4.3, 14	4.2, 16	4.2, 16
PCM	5	0,100	0, 100	0, 100	0, 100

After five thermal cycling experiments, the mass loss rates of MPCM-1 and PCM were 10% and 100%, respectively. At this stage, the PCMs rapidly melted and leaked during phase change. Meanwhile, the quality of MPCM-1 also decreased significantly because several PCMs were not completely coated inside the microcapsule, and some were only embedded in the grooves on the WM surface. After twenty thermal cycles, the mass loss rate of MPCM-1 was 16%. The mass loss rate of MPCM-1 increased slightly because most of the remaining PCMs at this stage underwent a phase transformation in the WM, and the morphology of the PCMs remained essentially stable. These results further verify that WM can effectively prevent the leakage of PCMs and ensure their heat storage density.

3.5. Heat Control Effect of MPCM-1

Figures 14 and 15 show the temperature change and hydration heat release of each cement slurry sample, respectively, as obtained using the self-made semi-adiabatic calorimeter.

Table 8 shows the values corresponding to the curves.

Table 8. Temperature and heat of hydration data for cement slurry.

Sample	T_i (°C)	T_m (°C)	ΔT (°C)	t_m (h)	Q_{20h} (J)	Q_m (J)
CS	11.3	31.3	20	16.6	49,812	61,729
$CSS_{10\%}$	10.2	28.1	17.9	18.1	37,583	46,555
$CSF_{10\%}$	10.7	26.5	15.8	16.8	32,954	40,,384
$CSM_{5\%}$	10.2	24.2	14.0	16.6	32,608	40618
$CSM1_{3\%}$	10.2	24.6	14.4	18.9	30,535	40,463
$CSM1_{5\%}$	10.7	22.4	11.7	19.8	25,410	38,212
$CSM1_{7\%}$	10.2	21.6	11.4	22.5	19,905	36,220

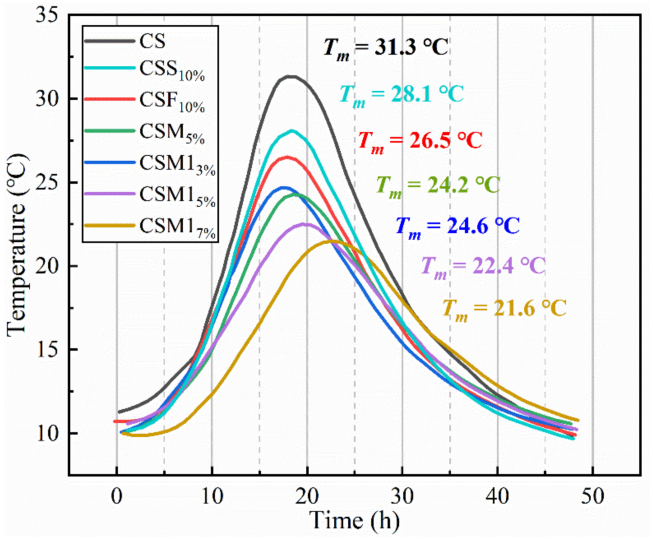

Figure 14. Hydration temperature of cement slurry samples.

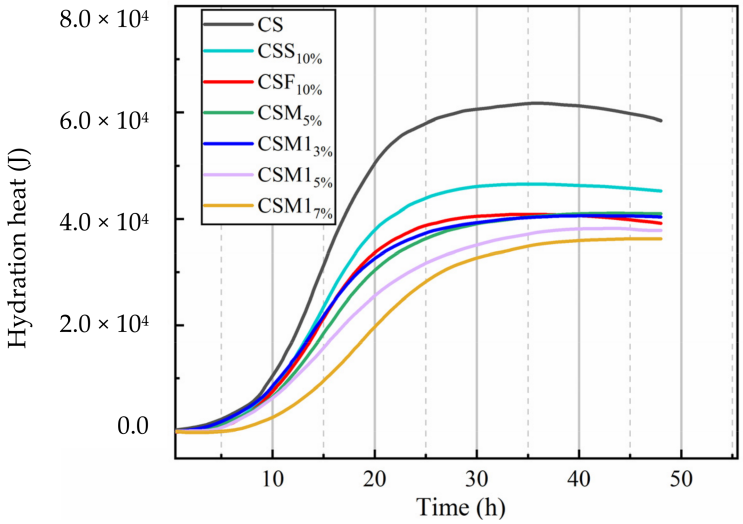

Figure 15. Hydration heat of cement slurry samples.

Compared to slag and fly ash, MPCM-1 has a more notable inhibitory effect on cement slurry temperature increase; this is reflected in the fact that the T_{max} of $CSM1_{7\%}$ was 6.5 °C and 4.9 °C lower than those of $CSS_{10\%}$ and $CSF_{10\%}$, respectively. Simultaneously, the T_{max} of $CSM1_{7\%}$ appeared later than those of $CSS_{10\%}$ and $CSF_{10\%}$. Similar results were also obtained in the research of Huo et al. [30]. They suggested that MPCM-1 not only replaced the active component of cement particles (similar to the function of slag and fly ash) but also absorbed heat released by the cement slurry during phase transformation. Compared to CSM, the maximum temperature and hydration heat of CSM1 were both lower, owing to the higher storage density of MPCM-1. In Figure 15 and Table 8, a significant positive correlation can be identified between the retarding effect of each low-heat material on the hydration heat release of the cement slurry; the effect of this on the temperature increase can also be seen. Moreover, the rate of increase in hydration heat for CSM1 was significantly faster than that for CS when the cement slurry temperature fell and approached the water bath temperature; this resulted from heat absorption during the liquid–solid phase transition of MPCM-1. Furthermore, compared with CS, the T_m and Q_m of $CSM1_{7\%}$ decreased by 9.7 °C and 25,509 J (41.3%), respectively, and T_m was extended by 5.9 h. The results show that MPCM-1 can effectively control the temperature increase and heat release rate of cement slurry, indicating that MPCM-1 has excellent prospects as a new additive for low-heat

cement slurry. Huo et al. [43] conducted a similar study. The results showed that the peak temperature of cement slurry decreased by 6 °C with 7.5% MPCM (prepared from urea-formaldehyde resin coated paraffin) dosage. The reasons why the ability of MPCM in the study of Huo et al. to regulate the temperature of cement slurry was worse than that of this study, is that MPCM-1 can quickly sense the temperature change in cement due to the incorporation of high thermal conductivity materials, and that PCMs' phase transition occurs in time to complete the endothermic process [44]. Here, T_i, T_m, and ΔT represent the initial temperature, maximum temperature, and maximum temperature difference for the cement slurry, respectively; furthermore, t_m denotes the time taken for the cement slurry to reach the maximum temperature. Q_{20h} and Q_m denote the heat release in 20 h and the final heat release of the cement slurry.

3.6. Comprehensive Strength of Cement Stone

In this section, the effects of MPCM-1, low-heat inorganic materials, and as-purchased microcapsules upon the comprehensive properties of cement stone are studied. As GHBS is soft and the pressure window between fracture and formation-pore pressure gradients is narrow, a low-density cement slurry system is usually used to cement the well to prevent loss of circulation [45–47]. As shown in Table 5, the reduction effect of MPCM-1 upon the initial density of cement slurry was more notable than other low-heat materials. Thus, the MPCM-1 cementing system conforms to this design philosophy [48]. Compared with CS, the fluidity of CSM1 decreased slightly within the allowable range. Wang et al. [39] found that the reason for the decrease in fluidity of cement slurry is that the particle size of MPCM is generally larger than that of cement particles, which enhances the friction between particles in cement slurry. The compressive strength of cement increased under the increase in MPCM-1 dosages within a certain range (see Figure 16).

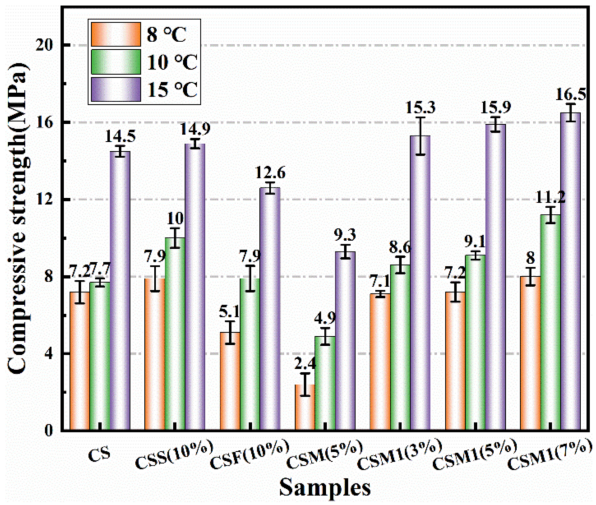

Figure 16. Compressive strength of cement stone after 24 h at 8 °C, 10 °C, and 15 °C.

Compared with CS, the compressive strength of $CSM1_{3\%}$, $CSM1_{5\%}$, and $CSM1_{7\%}$ cured at 15 °C for 24 h increased by 5.5%, 9.7%, and 13.8%, respectively. This occurs because PMMA (the shell of MPCM-1) is rigid; thus, it plays the role of an aggregate, which allows the cement stone of CSM1 to withstand higher external loads [49,50]. However, the results of Aguayo et al. [51] showed that a 5% dosage of microcapsules increased the number of pores in the cement stone, reducing its compressive strength by 12.5%. Ghods et al. [52,53] classified the pores inside the cement stone in terms of size and shape; they suggested that the macropores were the main factor affecting its compressive strength. Therefore, the reduction of large volume pores in cement stone may also represent an important factor when improving the compressive strength of CSM1. The spatial distribution of pores in the cement stone is studied in Section 3.7.

3.7. Distribution Analysis of MPCM-1 and Pores in Cement Stone

Figures 17 and 18 and Table 9 show the distribution of pores and MPCM-1 in cement stone, as obtained via micro-CT analysis.

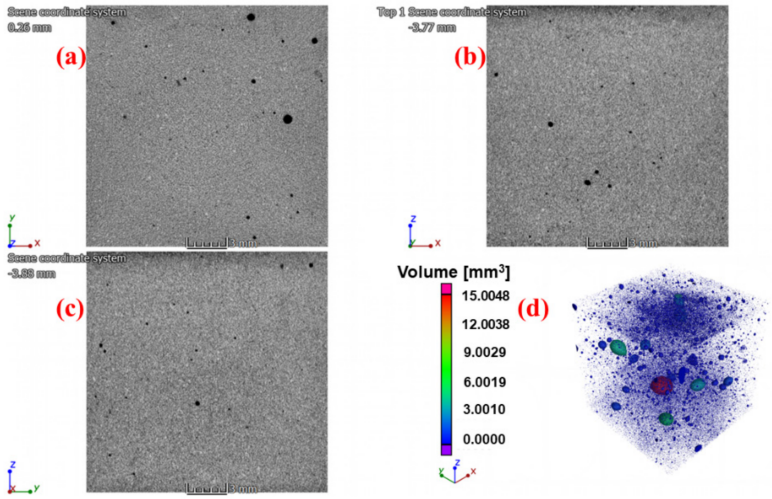

Figure 17. Slice images and 3D image model of the pores in CS.

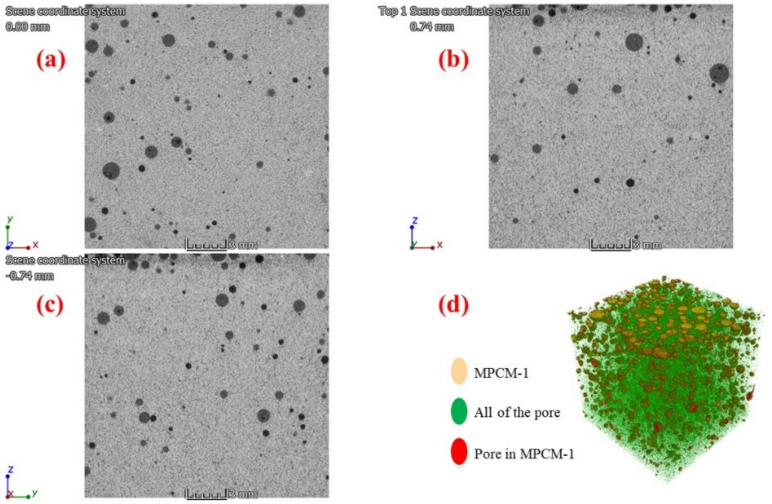

Figure 18. Slice images and 3D image model of the pores and MPCM-1 in $CSM1_{5\%}$.

Table 9. Total volume of MPCM-1, all pores, and the pores in MPCM-1.

Sample	CS	$CSM1_{5\%}$			
	Pore	MPCM-1	All Pores	Pores in MPCM-1	Pores in Cement
Total volume (mm^3)	62.4044	269.4997	98.7520	36.2646	62.4874

MPCM-1 is evenly distributed in the cement stone without agglomeration, which is amenable to the uniform heat control effect of MPCM-1 upon the cement slurry hydration process. Moreover, no clear arc-shaped pores (resulting from the incompatibility of MPCM-1 with cement slurry) were found around MPCM-1, and the porosity of cement in CSM1 was approximately equal to that of CS. Further, through reconstruction analyses, the volumes of MPCM-1 and its internal porosities were found to be 269.4997 mm^3 and 36.2646 mm^3, respectively. Calculated to be 13.4%, the porosity in MPCM-1 was already high, though it was lower than the true value, owing to accuracy limitations of the micro-CT scan.

Therefore, reducing the internal porosity of MPCM-1 should be considered in subsequent studies to improve its heat storage density and mechanical strength.

The voxel is the smallest volume unit that can be represented by a pixel after micro-CT reconstruction. The cumulative probability of voxel numbers in the pores inside the cement stone of CS and $CSM1_{5\%}$ is shown in Figure 19.

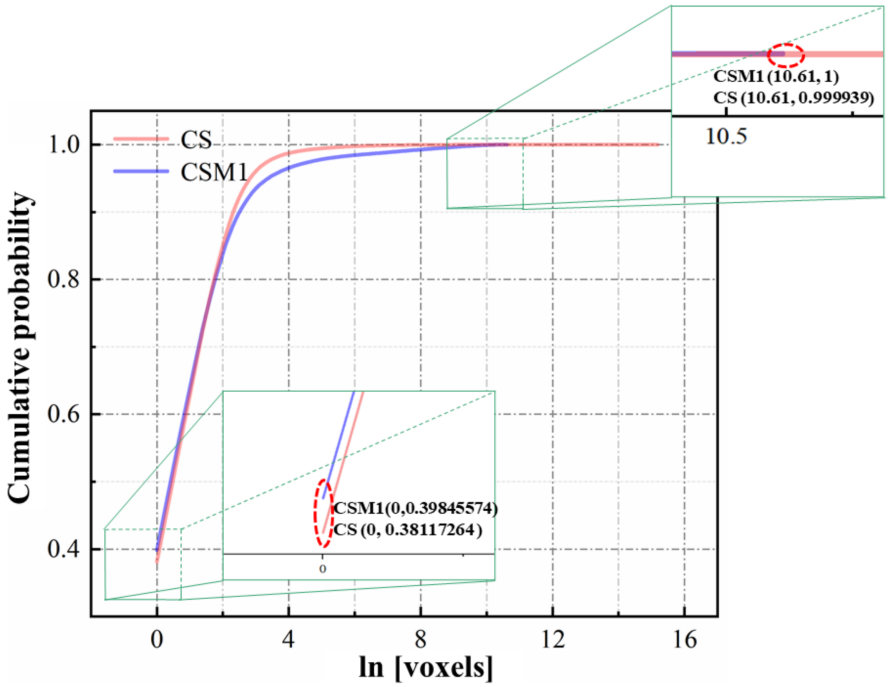

Figure 19. Cumulative probability of pore voxels in CS and $CSM1_{5\%}$ cement.

The voxel of the largest pore in $CSM1_{5\%}$ cement was 10.61 (i.e., 0.155 mm^3). Furthermore, it was calculated that 27 pores with a volume exceeding 0.155 mm^3 were present in CS, among which the maximum pore volume was 15.005 mm^3. Compared with CS, more small volume pores and fewer large volume pores were present in the cement stone of $CSM1_{5\%}$. Two factors may contribute to the reduction in the number of large volume pores: (1) the MPCM-1 increases the number of nucleation sites for the precipitation hydration products [39], and (2) the MPCM-1 (with a small particle size) plays a role in filling the pores. Therefore, MPCM-1 can (similar to defoamers) reduce the occurrence of large volume pores in the cement stone; this improves the mechanical strength of the cement stone [54,55]. Here, the side length of the unit voxel is 15.63 μm. Furthermore, micro-CT analysis at this precision shows that 447,743 and 501,657 pores are present in the CS and CSM1 cement stones, respectively.

3.8. Simulation of GHBS Damage

To further evaluate the protective function of a low-heat cement slurry system with MPCM-1 (to function as the key temperature control for GHBS stability), a device simulating the cementing operation of GHBS was designed and prepared (as shown in Figure 3). As the change in pressure during hydrate decomposition was considerably more drastic than the temperature change, the large pressure increase was selected as the standard by which to quantify the damage to GHBS stability.

The influence of the CS hydration heat on GHBS was observed, as shown in Figure 20.

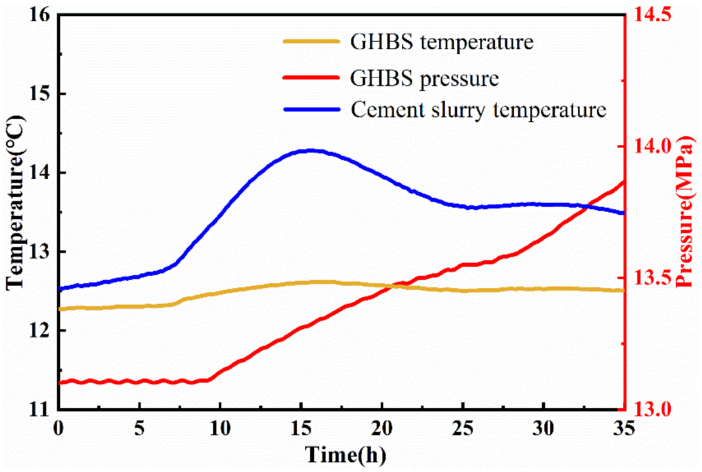

Figure 20. Damage of GHBS caused by hydration heat of CS.

In the first 7.5 h, owing to the slow increase of CS temperature in the initial hydration reaction [56], GHBS did not decompose under the thermal interaction between CS and GHBS. During this time, the temperature and pressure of GHBS remained essentially unchanged. Subsequently, the hydration process of CS entered an accelerated period [56], and the temperature increase in CS became more rapid. Owing to the enhanced heat exchange between CS and GHBS, the phase equilibrium condition for GHBS was destroyed, and the hydrate began to decompose. GHBS pressure increased significantly at 9.5 h, which continued until the end of the experiment, indicating that the stability of GHBS was completely damaged by the hydration heat release of CS.

As shown in Figure 21, under the hydration exothermic process of $CSM1_{5\%}$, the GHBS temperature and pressure began to increase significantly after 7 h via heat exchange between the CS and GHBS.

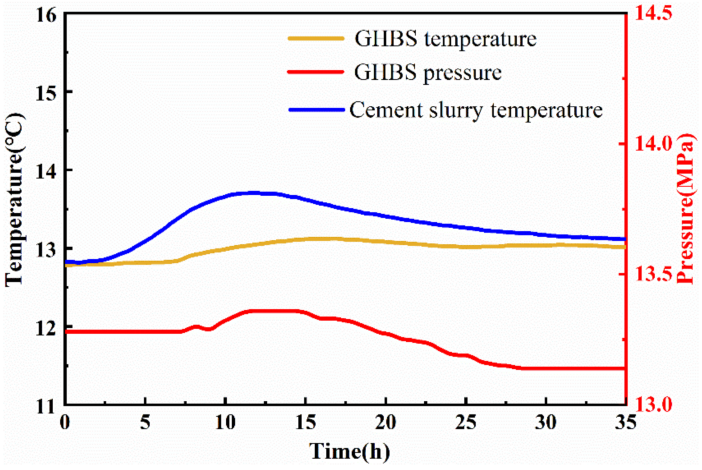

Figure 21. Damage of GHBS caused by hydration heat of $CSM1_{5\%}$.

When GHBS pressure reached the peak at 11.5 h, the ambient temperature and pressure were restored to the phase equilibrium via the pressure increase and temperature decrease caused by hydrate dissociation, after which the hydrate stopped decomposing. Meanwhile, the hydration exothermic rate of $CSM1_{5\%}$ gradually began to fall below the cooling rate, and the temperature of the cement slurry dropped. From 14.5 h, GHBS pressure began to decline until the GHBS reached a stable state at 28 h. At this stage, the GHBS pressure drop was attributable to re-formation of the lattice, in which the cavities that were trapped previously decomposed gas molecules and formed hydrate crystals. Compared to CS, the overall temperature increase rate of $CSM1_{5\%}$ was slower, and the temperature increased

less, which was conducive to the phase equilibrium recovery within the GHBS [2]. These results indicate that the addition of MPCM-1 can successfully reduce the damage to GHBS during heat release in cement slurry.

4. Conclusions

In this work, a new low-heat cement slurry system incorporating prepared phase change microcapsules (MPCM-1) was developed for cementing in natural gas hydrate-bearing sediment. The following conclusions can be drawn:

(1) The addition of lipophilic-modified graphite reduced the initial phase transition temperature of MPCM-1 by 0.49 °C, indicating that the sensitivity of MPCM-1 to temperature change was improved.
(2) MPCM-1 was superior to fly ash and slag for temperature regulation in the cement slurry hydration process.
(3) The addition of MPCM-1 reduced the number of large volume pores in the cement stone, which helped to improve the compressive strength of the cement stone.
(4) The self-made cementing simulation device test results show that the addition of MPCM-1 inhibits the temperature increase rate of cement slurry, significantly reducing the damage to natural gas hydrate-bearing sediment during cementing. This also intuitively confirms the feasibility of low-heat cement slurry systems with MPCM-1 (a key objective in the field).

This work not only provides a comprehensive and intuitive proof of the feasibility of the application of MPCM-doped low-temperature cement slurry in hydrate sediment cementing, but also provides a new idea for inhibiting the formation of temperature cracks in mass concrete in civil engineering.

Author Contributions: Conceptualization, Writing—Original draft preparation, Methodology: G.Y. Project administration: T.L. Project administration: H.Z. Validation: Z.Z. Visualization: Y.F. Conceptualization, Data Curation: E.L. Writing—Review and Editing: V.M. All authors have read and agreed to the published version of the manuscript.

Funding: This work was financed by the National Key Research and Development Program of China [Grant No. 2016YFE0204300] and the National Natural Science Foundation of China [Grant No. 42072343].

Informed Consent Statement: Not applicable.

Data Availability Statement: The study did not report any data.

Conflicts of Interest: The authors declare that they have no known competing financial interests or personal relationships that could have appeared to influence the work reported in this paper.

Abbreviations

GHBS	Natural gas hydrate-bearing sediment
MPCM	Microencapsulated phase-change materials
MG	Lipophilic-modified graphite
WM	Wall materials
C-S-H	Calcium silicate hydrate
CS	Control group cement slurry
$CSF_{10\%}$	CS incorporated with 10 wt% fly ash
$CSM1_{3\%}$	CS incorporated with 3 wt% MPCM-1
$CSM1_{7\%}$	CS incorporated with 7 wt% MPCM-1
T_o	The initial phase-change temperature, °C
T_e	The end phase-change temperature, °C
$\Delta H_{m(PCM)}$	The latent heat of PCM, J/g
T_i	The initial temperature of cement slurry, °C

ΔT	The maximum temperature difference of cement slurry, °C
Q_m	The final heat release of the cement slurry, J
PCMs	Phase-change materials
MPCM-1	Prepared heat-control microcapsule
MPCM-2	Prepared MG-free MPCM-1
MPCM-3	Phase-change microcapsule purchased from Shanghai Feikang Products Factory
PMMA	Polymethyl methacrylate
$CSS_{10\%}$	CS incorporated with 10 wt% slag
$CSM_{5\%}$	CS incorporated with 5 wt% MPCM-3
$CSM1_{5\%}$	CS incorporated with 5 wt% MPCM-1
D_n	Particle size when cumulative particle size distribution percentage reaches n%, mm
T_p	The peak phase-change temperature, °C
$\Delta H_{m(MPCM-1)}$	The latent heat of MPCM-1, J/g
E_e	The encapsulation efficiency of MPCM-1,%
T_m	The maximum temperature of cement slurry, °C
Q_{20h}	The heat release in 20 h of the cement slurry, J
t_m	Time when cement slurry reaches maximum temperature, h

References

1. Wang, X.; Sun, B.; Wang, Z.; Gao, Y.; Li, H. Coupled heat and mass transfer model of gas migration during well cementing through a hydrate layer in deep-water regions. *Appl. Therm. Eng.* **2019**, *163*, 114383. [CrossRef]
2. Liang, H.; Duan, Y.; Pei, J.; Wei, N. Study on Hydrate Phase Equilibrium Diagram of Methane Containing System Based on Thermodynamic Model. *Front. Energy Res.* **2021**, *9*, 743296. [CrossRef]
3. Zheng, M.; Liu, T.; Gao, Z.; Wu, J.; Jiang, G.; Li, Q.; Li, Z.; Xie, L. Simulation of natural gas hydrate formation skeleton with the mathematical model for the calculation of macro-micro parameters. *J. Pet. Sci. Eng.* **2019**, *178*, 429–438. [CrossRef]
4. Wang, X.; Sun, B.; Gao, Y.; Wang, Z.; Li, H.; Chen, Y. Numerical simulation of the stability of hydrate layer during well cementing in deep-water region. *J. Pet. Sci. Eng.* **2019**, *176*, 893–905. [CrossRef]
5. Sun, Y.; Wang, Y.; Guo, W.; Jia, R.; Chen, G.; Zhang, P. Hole-bottom freezing technique based on phase change heat transfer for gas-hydrates sampling: Efficiency optimization of refrigeration change of phase. *Appl. Therm. Eng.* **2018**, *130*, 722–734. [CrossRef]
6. Cohen, E.; Klar, A.; Yamamoto, K. Micromechanical Investigation of Stress Relaxation in Gas Hydrate-Bearing Sediments Due to Sand Production. *Energies* **2019**, *12*, 2131. [CrossRef]
7. Huo, J.-H.; Peng, Z.-G.; Feng, Q.; Zheng, Y.; Liu, X. Controlling the heat evaluation of cement slurry system used in natural gas hydrate layer by micro-encapsulated phase change materials. *Sol. Energy* **2018**, *169*, 84–93. [CrossRef]
8. Huo, J.-H.; Peng, Z.-G.; Ye, Z.-B.; Zuo, G.-L. Preparation, characterization and investigation of low hydration heat cement slurry system used in natural gas hydrate formation. *J. Pet. Sci. Eng.* **2018**, *170*, 81–88. [CrossRef]
9. Yang, G.; Liu, T.; Aleksandravih, B.P.; Wang, Y.; Feng, Y.; Wen, D.; Fang, C. Temperature regulation effect of low melting point phase change microcapsules for cement slurry in nature gas hydrate-bearing sediments. *Energy* **2022**, *253*, 124115. [CrossRef]
10. Yang, Y.; Wu, W.; Fu, S.; Zhang, H. Study of a novel ceramsite-based shape-stabilized composite phase change material (PCM) for energy conservation in buildings. *Constr. Build. Mater.* **2020**, *246*, 118479. [CrossRef]
11. Amirahmad, A.; Maglad, A.M.; Mustafa, J.; Cheraghian, G. Loading PCM Into Buildings Envelope to Decrease Heat Gain-Performing Transient Thermal Analysis on Nanofluid Filled Solar System. *Front. Energy Res.* **2021**, *9*, 727011. [CrossRef]
12. Costa, J.A.C.; Martinelli, A.E.; Nascimento, R.M.D.; Mendes, A. Microstructural design and thermal characterization of composite diatomite-vermiculite paraffin-based form-stable PCM for cementitious mortars. *Constr. Build. Mater.* **2020**, *232*, 117167. [CrossRef]
13. Mahdaoui, M.; Hamdaoui, S.; Msaad, A.A.; Kousksou, T.; El Rhafiki, T.; Jamil, A.; Ahachad, M. Building bricks with phase change material (PCM): Thermal performances. *Constr. Build. Mater.* **2020**, *269*, 121315. [CrossRef]
14. Coppola, L.; Coffetti, D.; Lorenzi, S. Cement-Based Renders Manufactured with Phase-Change Materials: Applications and Feasibility. *Adv. Mater. Sci. Eng.* **2016**, *2016*, 7254823. [CrossRef]
15. Memon, S.; Lo, T.Y.; Shi, X.; Barbhuiya, S.; Cui, H. Preparation, characterization and thermal properties of Lauryl alcohol/Kaolin as novel form-stable composite phase change material for thermal energy storage in buildings. *Appl. Therm. Eng.* **2013**, *59*, 336–347. [CrossRef]
16. Wang, R.; Kang, Y.; Lei, T.; Li, S.; Zhou, Z.; Xiao, Y. Microcapsules composed of stearic acid core and polyethylene glycol-based shell as a microcapsule phase change material. *Int. J. Energy Res.* **2021**, *45*, 9677–9684. [CrossRef]
17. Erdem, S.; Gürbüz, E. Influence of microencapsulated phase change materials on the flexural behavior and micromechanical impact damage of hybrid fibre reinforced engineered cementitious composites. *Compos. Part B Eng.* **2019**, *166*, 633–644. [CrossRef]

18. Hu, Y.; Guo, R.; Heiselberg, P.K.; Johra, H. Modeling PCM Phase Change Temperature and Hysteresis in Ventilation Cooling and Heating Applications. *Energies* **2020**, *13*, 6455. [CrossRef]
19. Huang, K.; Li, J.; Luan, X.; Liu, L.; Yang, Z.; Wang, C. Effect of Graphene Oxide on Phase Change Materials Based on Disodium Hydrogen Phosphate Dodecahydrate for Thermal Storage. *ACS Omega* **2020**, *5*, 15210–15217. [CrossRef]
20. Xie, N.; Niu, J.; Zhong, Y.; Gao, X.; Zhang, Z.; Fang, Y. Development of polyurethane acrylate coated salt hydrate/diatomite form-stable phase change material with enhanced thermal stability for building energy storage. *Constr. Build. Mater.* **2020**, *259*, 119714. [CrossRef]
21. Yan, T.; Li, T.; Xu, J.; Chao, J. Understanding the transition process of phase change and dehydration reaction of salt hydrate for thermal energy storage. *Appl. Therm. Eng.* **2020**, *166*, 114655. [CrossRef]
22. Li, Z.; Yuan, J. Phase change microcapsules with high encapsulation efficiency using Janus silica particles as stabilizers and their application in cement. *Constr. Build. Mater.* **2021**, *307*, 124971. [CrossRef]
23. Wu, R.; Gao, W.; Zhou, Y.; Wang, Z.; Lin, Q. A novel three-dimensional network-based stearic acid/graphitized carbon foam composite as high-performance shape-stabilized phase change material for thermal energy storage. *Compos. Part B Eng.* **2021**, *225*, 109318. [CrossRef]
24. Wang, X.; Chen, Z.; Xu, W.; Wang, X. Capric acid phase change microcapsules modified with graphene oxide for energy storage. *J. Mater. Sci.* **2019**, *54*, 14834–14844. [CrossRef]
25. Chen, C.; Chen, J.; Jia, Y.; Topham, P.D.; Wang, L. Binary shape-stabilized phase change materials based on poly(ethylene glycol)/polyurethane composite with dual-phase transition. *J. Mater. Sci.* **2018**, *53*, 16539–16556. [CrossRef]
26. Khetib, Y.; Alahmadi, A.A.; Alzaed, A.; Sajadi, S.M.; Cheraghian, G.; Sharifpur, M. Numerical study of the effect of graphene nanoparticles in calcium chloride hexahydrate -based phase change material on melting and freezing time in a circular cavity with a triangular obstacle. *J. Energy Storage* **2021**, *43*, 103243. [CrossRef]
27. Sarı, A.; Saleh, T.A.; Hekimoğlu, G.; Tyagi, V.; Sharma, R. Microencapsulated heptadecane with calcium carbonate as thermal conductivity-enhanced phase change material for thermal energy storage. *J. Mol. Liq.* **2021**, *328*, 115508. [CrossRef]
28. Yu, S.; Wang, X.; Wu, D. Microencapsulation of n-octadecane phase change material with calcium carbonate shell for enhancement of thermal conductivity and serving durability: Synthesis, microstructure, and performance evaluation. *Appl. Energy* **2014**, *114*, 632–643. [CrossRef]
29. Liu, X.; Feng, Q.; Peng, Z.; Zheng, Y.; Liu, H. Preparation and evaluation of micro-encapsulated thermal control materials for oil well cement slurry. *Energy* **2020**, *208*, 118175. [CrossRef]
30. Huo, J.-H.; Peng, Z.-G.; Xu, K.; Feng, Q.; Xu, D.-Y. Novel micro-encapsulated phase change materials with low melting point slurry: Characterization and cementing application. *Energy* **2019**, *186*, 115920. [CrossRef]
31. Aguayo, M.; Das, S.; Maroli, A.; Kabay, N.; Mertens, J.C.; Rajan, S.D.; Sant, G.; Chawla, N.; Neithalath, N. The influence of microencapsulated phase change material (PCM) characteristics on the microstructure and strength of cementitious composites: Experiments and finite element simulations. *Cem. Concr. Compos.* **2016**, *73*, 29–41. [CrossRef]
32. Xie, W.; Guo, S.; Liu, Y.; Chen, R.; Wang, Q. Organic-inorganic hybrid strategy based on ternary copolymerization to prepare flame retardant poly(methyl methacrylate) with high performance. *Compos. Part B Eng.* **2020**, *203*, 108437. [CrossRef]
33. Zhu, B.; Huang, X.; Guo, Y. Influence of Cement Particle Size Distribution on Strength of Cement Paste. In *Advanced Engineering Materials*; Zeng, J.M., Li, T.S., Ma, S.J., Jiang, Z.Y., Yang, D.G., Eds.; Pts 1-32011; Trans Tech Publications: Zurich, Switzerland, 2011; pp. 1007–1011.
34. Qiao, D.; Cheng, W.; Xie, J.; Wang, J.; Huang, F.; Mo, Y.; Peng, J. Analysis of the influence of gradation on the strength of a cemented filling body and the cementation strength model. *Integr. Ferroelectr.* **2019**, *199*, 12–21. [CrossRef]
35. Althoey, F.; Zaid, O.; De-Prado-Gil, J.; Palencia, C.; Ali, E.; Hakeem, I.; Martínez-García, R. Impact of sulfate activation of rice husk ash on the performance of high strength steel fiber reinforced recycled aggregate concrete. *J. Build. Eng.* **2022**, *54*, 104610. [CrossRef]
36. Zhang, R.; Zhang, W.; Shi, M.; Li, H.; Ma, L.; Niu, H. Morphology controllable synthesis of heteroatoms-doped carbon materials for high-performance flexible supercapacitor. *Dyes Pigment.* **2022**, *199*, 109968. [CrossRef]
37. Tondro, H.; Zilouei, H.; Zargoosh, K.; Bazarganipour, M. Nettle leaves-based sulfonated graphene oxide for efficient hydrolysis of microcrystalline cellulose. *Fuel* **2020**, *284*, 118975. [CrossRef]
38. Zhou, D.; Zhou, Y.; Liu, Y.; Luo, X.; Yuan, J. Preparation and Performance of Capric-Myristic Acid Binary Eutectic Mixtures for Latent Heat Thermal Energy Storages. *J. Nanomater.* **2019**, *2019*, 2094767. [CrossRef]
39. Wang, Y.; Li, J.; Miao, W.; Su, Y.; He, X.; Strnadel, B. Preparation and characterizations of hydroxyapatite microcapsule phase change materials for potential building materials. *Constr. Build. Mater.* **2021**, *297*, 123576. [CrossRef]
40. Sha, Z.; Liang, J.; Zhang, G.; Yang, S.; Lu, J.; Zhang, Z.; McConnell, D.R.; Humphrey, G. A seepage gas hydrate system in northern South China Sea: Seismic and well log interpretations. *Mar. Geol.* **2015**, *366*, 69–78. [CrossRef]
41. Wu, X.; Liang, Q.; Ma, Y.; Shi, Y.; Xia, Z.; Liu, L.; Haeckel, M. Submarine Landslides and their Distribution in the Gas Hydrate Area on the North Slope of the South China Sea. *Energies* **2018**, *11*, 3481. [CrossRef]
42. Zhou, D.; Yuan, J.; Zhou, Y.; Liu, Y. Preparation and Properties of Capric–Myristic Acid/Expanded Graphite Composite Phase Change Materials for Latent Heat Thermal Energy Storage. *Energies* **2020**, *13*, 2462. [CrossRef]
43. Huo, J.-H.; Peng, Z.-G.; Feng, Q.; Zheng, Y.; Zhang, J. Controlling the heat evolution of cement slurry system using microencapsulated phase change materials. *Int. J. Energy Res.* **2018**, *42*, 4206–4220. [CrossRef]

44. Zhao, C.; Opolot, M.; Liu, M.; Bruno, F.; Mancin, S.; Hooman, K. Phase change behaviour study of PCM tanks partially filled with graphite foam. *Appl. Therm. Eng.* **2021**, *196*, 117313. [CrossRef]
45. Ravi, K.; Iverson, B.; Moore, S. Cement-Slurry Design to Prevent Destabilization of Hydrates in Deepwater Environment. *SPE Drill. Complet.* **2009**, *24*, 373–377. [CrossRef]
46. Yue, J.; Liu, Z.; Wang, J.; Sun, T.; Wu, Z.; Geng, Y. A Low-Cost and Low-Density Cement Slurry System Suitable for a Shallow Unconsolidated Stratum. *Adv. Mater. Sci. Eng.* **2020**, *2020*, 1628281. [CrossRef]
47. Zheng, M.; Liu, T.; Jiang, G.; Wei, M.; Huo, Y.; Liu, L. Large-scale and high-similarity experimental study of the effect of drilling fluid penetration on physical properties of gas hydrate-bearing sediments in the Gulf of Mexico. *J. Pet. Sci. Eng.* **2019**, *187*, 106832. [CrossRef]
48. Nikolaev, N.; Saint Petersburg Mining University; Leusheva, E. Low-Density Cement Compositions for Well Cementing Under Abnormally Low Reservoir Pressure Conditions. *J. Min. Inst.* **2019**, *236*, 194–200. [CrossRef]
49. Berodier, E.; Scrivener, K. Understanding the Filler Effect on the Nucleation and Growth of C-S-H. *J. Am. Ceram. Soc.* **2014**, *97*, 3764–3773. [CrossRef]
50. Nikolaev, N.I.; Haoya, L. Results of "Cement-to-Rock" Contact Study. *J. Min. Inst.* **2017**, *226*, 428–434.
51. Fernandes, F.; Manari, S.; Aguayo, M.; Santos, K.; Oey, T.; Wei, Z.; Falzone, G.; Neithalath, N.; Sant, G. On the feasibility of using phase change materials (PCMs) to mitigate thermal cracking in cementitious materials. *Cem. Concr. Compos.* **2014**, *51*, 14–26. [CrossRef]
52. Ghods, P.; Isgor, O.; Carpenter, G.; Li, J.; McRae, G.; Gu, G. Nano-scale study of passive films and chloride-induced depassivation of carbon steel rebar in simulated concrete pore solutions using FIB/TEM. *Cem. Concr. Res.* **2013**, *47*, 55–68. [CrossRef]
53. Li, L.; Liu, T.; Jiang, G.; Zheng, S.; Fang, C.; Sun, J.; Qu, B.; Zhu, Y. Interactive mechanism of manufacturing factors on the properties of microbial cementing slurry. *Constr. Build. Mater.* **2021**, *311*, 125308. [CrossRef]
54. Bu, J.; Tian, Z.; Zheng, S.; Tang, Z. Effect of sand content on strength and pore structure of cement mortar. *J. Wuhan Univ. Technol. Sci. Ed.* **2017**, *32*, 382–390. [CrossRef]
55. Li, L.; Liu, T.; Jiang, G.; Fang, C.; Sun, J.; Zheng, S.; Liu, H.; Leusheva, E.; Morenov, V.; Nikolaev, N. Field Application of Microbial Self-Healing Cement Slurry in Chunguang 17-14 Well. *Energies* **2021**, *14*, 1544. [CrossRef]
56. Bullard, J.W.; Jennings, H.M.; Livingston, R.; Nonat, A.; Scherer, G.; Schweitzer, J.S.; Scrivener, K.; Thomas, J. Mechanisms of cement hydration. *Cem. Concr. Res.* **2011**, *41*, 1208–1223. [CrossRef]